WILEY-VCH

DOI: 10.1002/201703261
Article Type: Full Paper

$Na_3V_2(PO_4)_3$/C Positive Electrodes with High Energy and Power Densities for Sodium Secondary Batteries with Ionic Liquid Electrolytes that Operate Across Wide Temperature Ranges

*Jinkwang Hwang, Kazuhiko Matsumoto,** and *Rika Hagiwara*

J. Hwang, Prof. K. Matsumoto,* Prof. R. Hagiwara
Graduate School of Energy Science, Kyoto University
Yoshida-honmachi, Sakyo-ku, Kyoto 606-8501, Japan
E-mail: k-matsumoto@energy.kyoto-u.ac.jp

Prof. K. Matsumoto,* Prof. R. Hagiwara
Unit of Elements Strategy Initiative for Catalysts & Batteries (ESICB), Kyoto University
Katsura, Kyoto 615-8510, Japan

Keywords: Sodium secondary batteries, NASICON, Ionic liquids, High rate capability, Wide temperature range

Positive electrode materials with a wide operating temperature range and high energy and power densities are required for the construction of practical sodium secondary batteries. High performance is expected at elevated temperatures because electrode reactions and ion diffusion are enhanced under such conditions. In the present study, carbon-coated NASICON-type $Na_3V_2(PO_4)_3$ is prepared via a sol-gel method and investigated as a positive electrode material for sodium secondary batteries operating under low-to-intermediate temperature conditions. The $Na_3V_2(PO_4)_3$/C material utilizes fully the safety and large liquid-phase temperature range of Na[FSA]-[C_2C_1im][FSA] (C_2C_1im = 1-ethyl-3-methylimidazolium, FSA = bis(fluorosulfonyl)amide) ionic liquid electrolytes. Electrochemical testing of the $Na_3V_2(PO_4)_3$/C composite reveal superior cycling and rate performance at 253–363 K. Cycling tests at 1C (117 mA g^{-1}) confirm capacity retention of 99% and Coulombic efficiency of over 99.9% after 300 cycles at 298 K and 363 K. Even faster-current cycling at 20C results in capacity retention of 89.2% after 5000 cycles at 363 K. The high rate capability at 363 K (50.1 mAh g^{-1} at 58500 mA g^{-1}) leads to excellent power and energy densities that exceed those of $NaCrO_2$ and $Na_2FeP_2O_7$.

1. Introduction

The popularity of renewable electricity generation has increased over the last years as the application of the relevant technologies has become more feasible. However, intermittent production of electricity by renewable energy sources such as solar and wind power and variable demand cause significant problems for electrical grids. Therefore, energy storage systems (ESSs) are essential for the development of large-scale power supply networks.[1] Of the ESSs currently proposed for large-scale stationary applications, e.g., pumped-storage hydroelectricity, flywheels, and etc.,[1b, 2] secondary batteries are particularly attractive owing to their high power and energy densities, pollution-free operation, high efficiency, simple maintenance, and versatility. Thus far, Li secondary batteries offer the best balance in terms of energy and power densities.[1b, 2-3] In fact, several devices based on Li secondary batteries have already been commercialized as a result of their high performance. For the past two decades, these devices had a large share in the global secondary battery market. However, Li resources are limited and unevenly distributed (located primarily in South America).[4] This limitation is expected to become a significant obstacle to the mass production of large-scale Li secondary batteries in the near future.

Sodium secondary batteries are among the most promising large-scale ESS candidates. These batteries are appealing because sodium is abundant and available worldwide, and the standard redox potential is sufficiently negative.[5] The sodium has the second smallest ionic radius of the group 1 elements[6] (in the case of 6-coordination, 1.02 Å for Na^+ and 0.76 Å for Li^+ [7]), which is important when designing electrode materials that are analogous to those made using Li counterparts. Despite these valuable features, however, Na secondary batteries are typically not used in real applications because the currently available electrode-active materials and electrolytes suffer from limitations in terms of performance, safety, and cost. Since the primary application for Na secondary batteries is large-scale energy storage, high

charge/discharge rates, cycling stability, ability to operate across a wide range of temperatures, safety, and cost are critical requirements. In an effort to satisfy these requirements, several polyanionic compounds such as $Na_2FeP_2O_7$, Na_2FePO_4F, and $NaFePO_4$ have been studied as positive electrode materials for Na secondary batteries.[8]

Polyanionic compounds with tetrahedral polyanion units, $(XO_4)^{n-}$ (X = P, S, Si, As, Mo, or W) can combine with MO_x (M = transition metal) polyhedral units to form structural frameworks. Phosphate-based electrode materials offer open frameworks that favor facile Na^+ ion transport.[9] Among these phosphate compounds, Na superionic conductor (NASICON)-type $Na_3V_2(PO_4)_3$ (NVP) is well known for its high Na-ion conductivity, which originates from the corner-sharing arrangement of the polyhedral units. The NVP has been proposed as a positive electrode material based on the V^{3+}/V^{4+} redox reaction, and offers a theoretical capacity of 117.6 mAh g^{-1} ($Na_3V_2(PO_4)_3 \rightleftarrows NaV_2(PO_4)_3 + 2Na^+ + 2e^-$). Its high thermal stability enables operation across a wide temperature range. In previous studies, however, this material has exhibited poor cyclability and rate capabilities as a result of its low electrical conductivity at room temperature.[10] Rate capability improvements have been reported using an ionic liquid (IL) electrolyte at 353 K in a symmetrical cell (V^{3+}/V^{4+}–V^{3+}/V^{2+})[10e], however, practical performance has not been pursued using IL since then. Recent studies have reported that this material exhibits high cyclability and rate performance in organic electrolytes when prepared via carbon coating.[10a-d, 11]

Figure 1 shows the operating temperatures of secondary batteries required for various applications. Although batteries designed for hot environments such as those implemented in rescue robots and measurement equipment for drilling applications have been studied, studies directed at examining the utilization of waste heat or hot environments to improve battery performance are rare.[12] Hot environments are ubiquitous in our daily lives and in industrial settings, and include, for example, automobile engine compartments and heavy-industrial settings involving waste heat and waste treatment plants. The efficient use of such heat

represents a potential way of achieving high performance with either known or unknown electrode materials. Furthermore, batteries for electric vehicles (EVs), hybrid electric vehicles (HEVs), and various other applications must operate across a wide range of temperatures. Unfortunately, organic electrolytes can only be used over a limited temperature range (<60 °C) as a result of their flammabilities and volatilities, which are the main causes of recent lithium-ion battery (LIB) safety issues.[13]

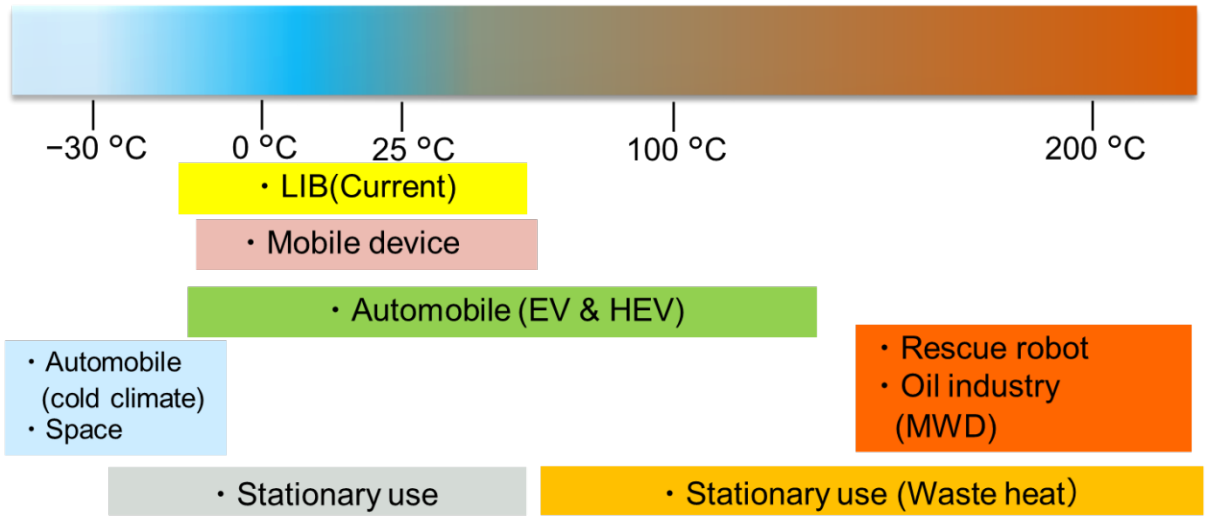

Figure 1 Operating temperature ranges of various secondary batteries and the temperatures required for selected applications.

In addition, co-solvents and additives are required for the use of organic electrolytes at low temperatures.[13a, 14] ILs composed of only cations and anions are non-flammable, as well as chemically, electrochemically, and thermally stable, and exhibit wide electrochemical windows.[15] Thus, such ILs can be used as electrolytes in secondary batteries designed for use from subfreezing to intermediate temperatures. Previously, examination of basic physical properties was reported for the purposes of advancing battery applications,[16] along with an overview of practical applications of ILs, including Na secondary batteries.[17] In our previous work, we examined the intermediate-temperature operation of Na secondary batteries with an FSA-based (FSA = bis(fluorosulfonyl)amide) IL electrolyte with a range of positive (e.g., $NaCrO_2$, $Na_2FeP_2O_7$, and $NaFePO_4$)[18] and negative electrode (Sn, metal-Sn alloy, and hard

carbon) materials.[19] FSA-based ILs are more stable than other ILs against reduction in both Li and Na systems with various other popular anions, and across a wide temperature range.[20] These ILs are suitable for operation of Na secondary batteries at intermediate temperatures.[20c, 21] Intermediate temperature operation exploiting the use of waste heat and hot environments can potentially enhance Na^+ ion transport and electrode reactions, enabling thus increased practical capacities, as well as excellent cyclabilities and rate capabilities.[18b, 22]

In this work, the electrochemical properties of carbon-coated $Na_3V_2(PO_4)_3$ (NVPC) electrodes prepared via a sol-gel method are tested at various temperatures using the Na[FSA]-[C_2C_1im][FSA] (C_2C_1im = 1-ethyl-3-methylimidazolium) IL system with Na[FSA] molar fractions ranging from 0.1 to 0.5[23] in order to develop Na secondary batteries that operate from subfreezing to intermediate temperatures. In addition, intermediate-temperature sodiation/desodiation mechanisms in the NVPC structure are analyzed via *in-situ* X-ray diffraction (XRD) measurements. Finally, relationships between energy and power densities are compared to those of existing positive electrode materials ($NaCrO_2$ and $Na_2FeP_2O_7$) to confirm the effectiveness of the present system.

2. Results and Discussion

2.1. Structural Characteristics

The XRD patterns of the synthesized NVPC electrodes confirm the presence of a pure NVP phase and an amorphous carbon phase. The XRD pattern of NVPC was indexed as a rhombohedral crystal system, and was fitted with space group $R\bar{3}c$ via Rietveld refinement. The lattice parameters of the NVPC were determined to be a = 8.72209(12) and 21.8563(5) Å (R_{wp} = 16.0), and match the crystallographic data from previous reports[11c] (see **Figure 2** and Table S1 in the Supporting Information for crystallographic data). The XRD pattern of NVPC matches that of NVP prepared by a solid-state method (NVP-SS) (inset of Figure 2), although the former exhibits slightly broader diffraction peaks.

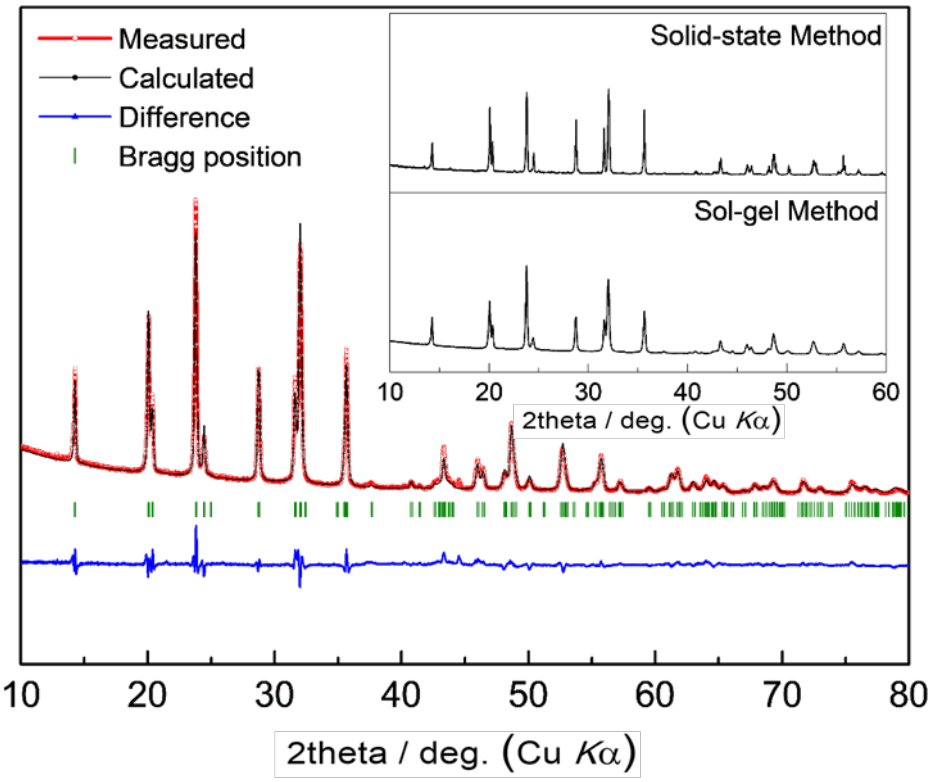

Figure 2 Rietveld refinement results for NVPC prepared via a sol-gel method and XRD analysis of NVP synthesized via a solid-state method (inset). See Table S1 for details of NVPC crystallographic data.

The scanning electron microscopy (SEM) image and energy-dispersive X-ray spectrometry (EDS) map of NVPC powder are shown in **Figure 3**. The synthesized NVPC composites are composed of particles of various sizes, which produce a porous, coral-reef morphology. The magnified SEM images (Figure S1) show a number of particles around 50 nm in size within the pores of the bulk NVPC particles, while NVP-SS has a particle size of around 25 μm, and exhibits non-porous morphology (Figure S2). The specific surface areas obtained by the Brunauer–Emmett–Teller (BET) method revealed that NVPC has surface area that is 100 times larger than that of NVP-SS. Control over the morphology and the application of homogeneous carbon coating are critical for the good electrochemical performance of NVPC since the numbers of active sites and diffusion paths are highly related to the electrode reaction. EDS mapping results matched the expected composition of NVPC, with all elements

distributed over the particles. The actual carbon content in NVPC was determined to be 10.8 wt% via elemental analysis.

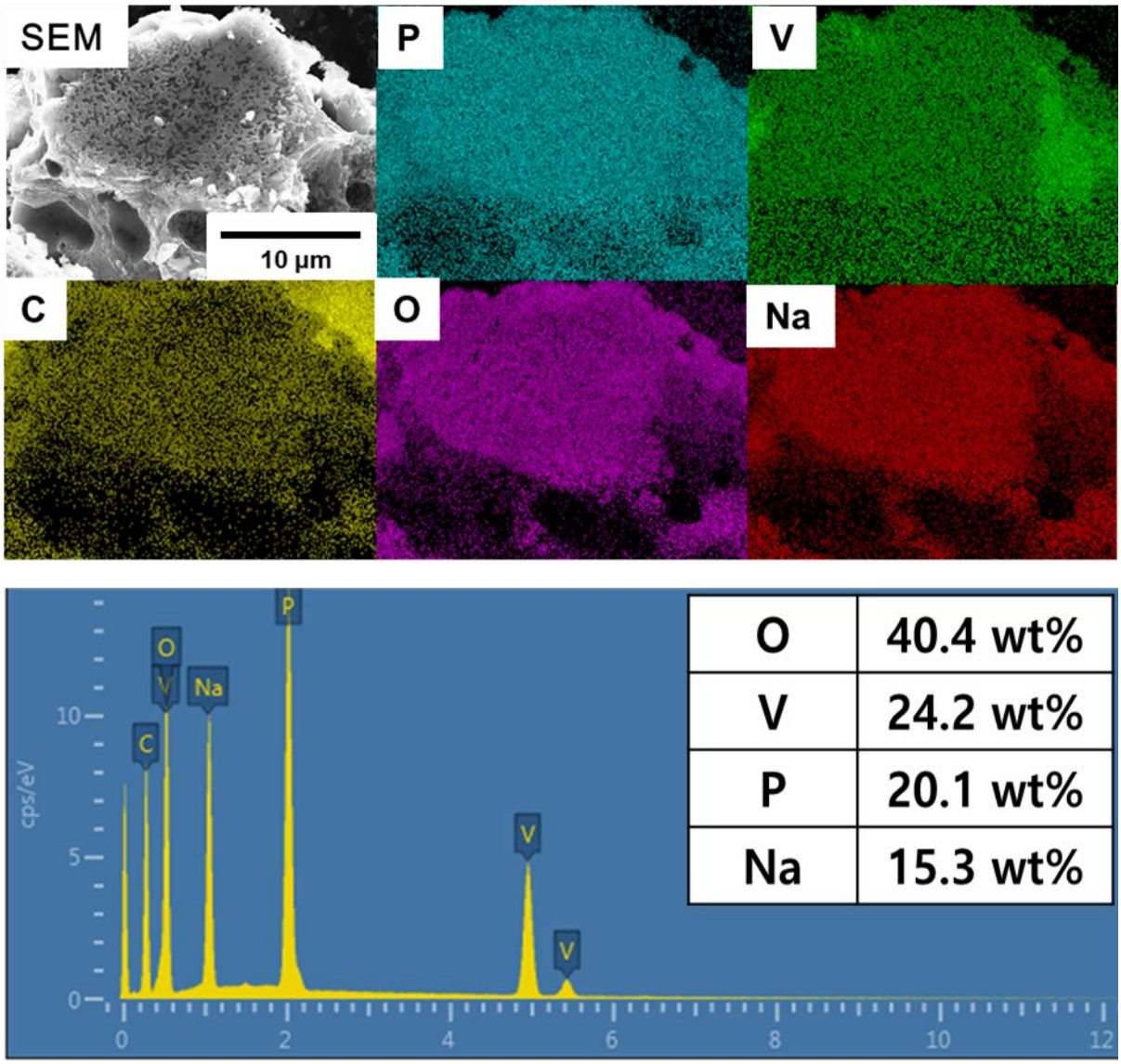

Figure 3 SEM image and EDS map of elements present in the NVPC sample. The amount of carbon was omitted from the calculation of elemental composition by weight.

2.2. Electrochemical Characterization

2.2.1. Charge–Discharge Behavior

Figure 4 shows galvanostatic charge–discharge curves of Na/NVP-SS and Na/NVPC cells at 0.1C using the Na[FSA]-[C_2C_1im][FSA] (Na[FSA] mole fraction = 0.5) IL electrolyte. The NVP-SS cell exhibits a first-discharge reversible capacity of only 44.3 mAh g^{-1} at 298 K. This reversible capacity degrades rapidly, reaching 34.0 mAh g^{-1} on the fifth cycle (Figure 4

(a)). As the temperature increases, the NVP-SS cell exhibits a slightly larger first discharge capacity of 50.6 mAh g^{-1} at 363 K. However, similarly to the behavior observed at 298 K, the capacity degrades rapidly, reaching 38.7 mAh g^{-1} on the fifth cycle [Figure 4 (b)]. The limited performance described here occurs as a result of the characteristic low electrical conductivity of NVP-SS.

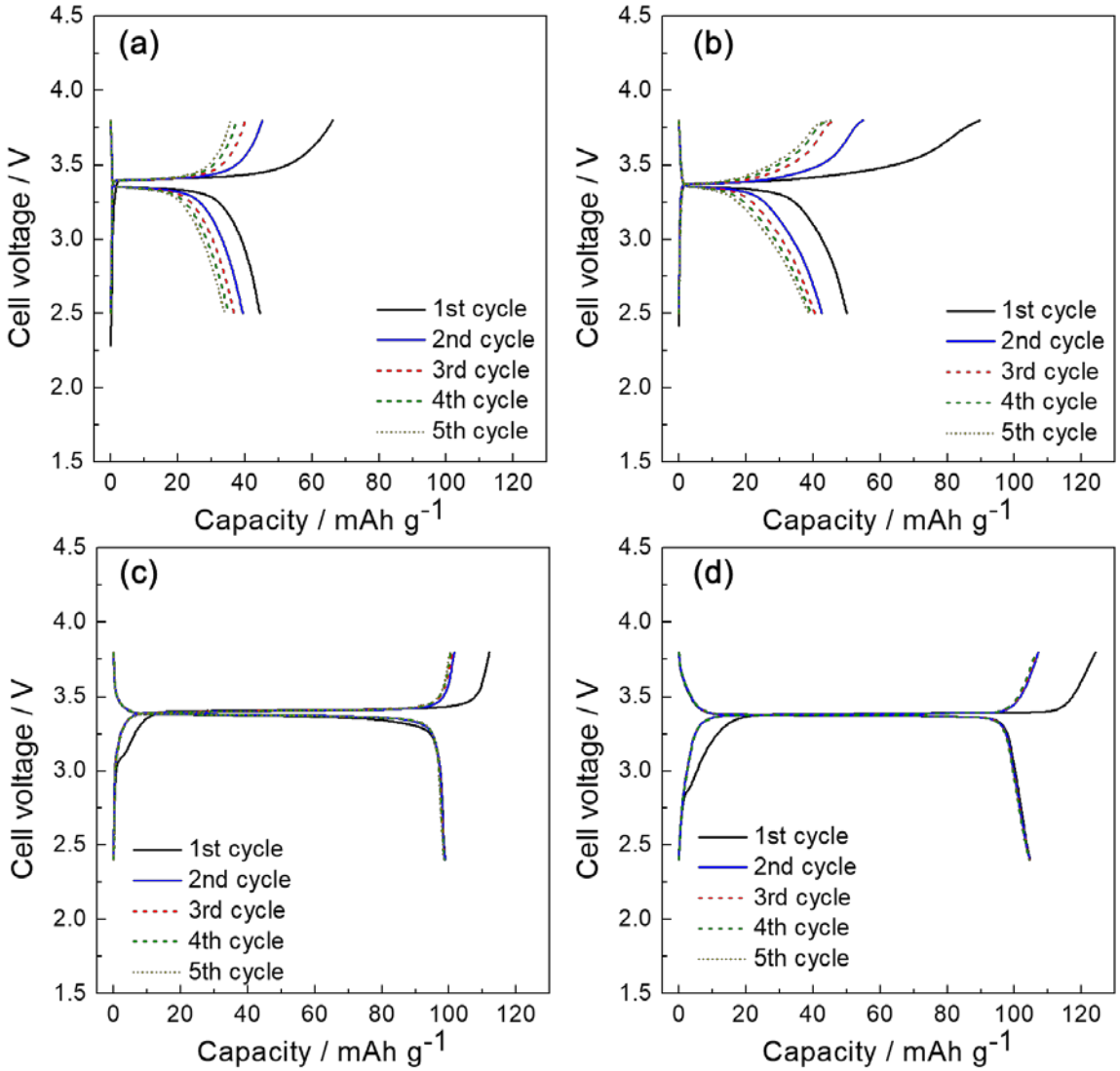

Figure 4 Charge–discharge curves of Na/NVP cells at (a) 298 K and (b) 363 K; and Na/NVPC cells at (c) 298 K and (d) 363 K. Electrolyte: Na[FSA]-[C_2C_1im][FSA] (Na[FSA] mole fraction = 0.5). The charge–discharge rate and cut-off voltages are 0.1C, and 2.4 V/3.8 V, respectively.

The charge–discharge performance improves dramatically after carbon coating. The NVPC composite exhibits reversible capacities of 98.7 mAh g^{-1} and 104.5 mAh g^{-1} at 298 K [Figure 4 (c)] and 363 K [Figure 4 (d)], respectively. During charging and discharging, a flat

plateau is observed at approximately 3.4 V. This is associated with the V^{4+}/V^{3+} redox activity ($NaV_2(PO_4)_3/Na_3V_2(PO_4)_3$) seen in organic electrolytes.[24] Capacities of about 100 mAh g^{-1} are obtained at 298 K regardless of the Na[FSA] mole fraction used. Increasing the temperature increases the capacity slightly (see Figures S4 and S5 in the Supporting Information for charge–discharge profiles with different molar ratios).

2.2.2. Rate Capability and Super-Fast Rate Capability

Prior studies reported that NVP fabricated with carbonaceous materials can exhibited improved rate capabilities in organic electrolytes.[11a, 11c, 24] Graphene-scaffolded NVP with 1.0-mol L^{-1} $NaClO_4$ dissolved in ethylene carbonate/diethyl carbonate (EC/DEC, 1:1, v/v) as the electrolyte exhibited a capacity of 44 mAh g^{-1} at 50C.[11a] Carbon-coated, porous NVP using a 1-M $NaClO_4$ in ethylene carbonate and propylene carbonate (1:1, v/v) as the electrolyte exhibited a capacity retention of 54% at 40C.[24] Another carbon-coated porous NVP using an electrolyte comprised of 1-M $NaClO_4$ in propylene carbonate and 2% fluorinated ethylene carbonate exhibited a capacity of 75.54 mAh g^{-1} at 80C.[11c] Such superior NVP rate performance was further improved upon via intermediate-temperature operation with IL electrolytes in the present study.

Figure 5 compares the rate capabilities of Na/NVPC cells at 298 K and 363 K. The cells examined were prepared using the Na[FSA]-[C_2C_1im][FSA] system at four different Na[FSA] mole fractions. The cells are charged up to 3.8 V at a constant current of 0.1C and then discharged to 2.4 V at 0.1–40C. At both temperatures, the discharge capacity decreases as the discharge current increases, regardless of the Na[FSA] mole fraction in the IL. The highest capacity retention at 20C is observed with Na[FSA] mole fractions of 0.2 and 0.5 at 298 K (40.3%) and 363 K (93.0%), respectively. These results suggest that the rate capability improves significantly at 363 K and the Na[FSA] fraction for which the highest capacity retention is observed differs as a function of temperature (see Figures S6 and S7 in the

Supporting Information for discharge curves during rate capability tests with ILs containing different mole fractions of Na[FSA]).

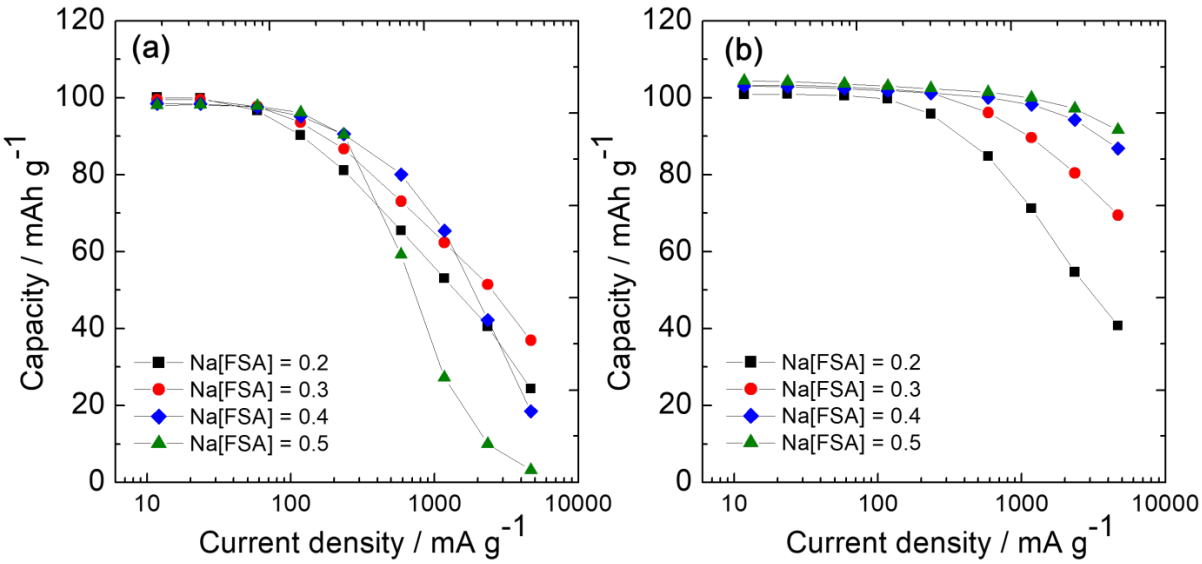

Figure 5 Rate capabilities of Na/NVPC cells at (a) 298 K and (b) 363 K. Electrolyte: Na[FSA]-[C_2C_1im][FSA] (Na[FSA] mole fraction = 0.2−0.5). Charge rate: 0.1C, discharge rates: 0.1C to 40C, cut-off voltages: 2.4 V/3.8 V. See Figures S6 and S7 in the Supporting Information for the discharge curves.

The Na/NVPC cells displayed markedly higher rate capabilities at elevated temperatures, and, thus, further high-rate charge–discharge tests were performed using cells with high Na[FSA] contents. **Figure 6** shows the results of super-fast rate capability tests of a Na/NVPC cell with an Na[FSA] fraction of 0.5 at 363 K. The cell was charged to 3.8 V at a constant current of 0.1C and then discharged to 2.4 V at currents ranging from 0.1C to 700C. A discharge rate of 700C corresponds to 81900 mA g^{-1} and a 5.1 s discharge (see Table S2 in the Supporting Information for the capacities and capacity retention values depicted in Figure 6). Up to a discharge rate of 100C, the cells exhibit capacity retentions of at least 80% of the values achieved at 0.1C. Moreover, capacity retentions of 48%, 35%, and 23% are obtained at 500C, 600C, and 700C, respectively. The polarization increases as the current density increases, which leads to the large capacity loss at high current densities. Thus, different lower cut-off voltages (0.8-2.4 V) were applied to confirm the possible increase in capacity (see Figure S8 and Table S3). The results show that discharge capacities increase after

adjusting the cut-off voltages—capacity retentions of 69%, 58%, 36%, and 19% are obtained at 500C, 1000C, 1600C, and 2000C, respectively.

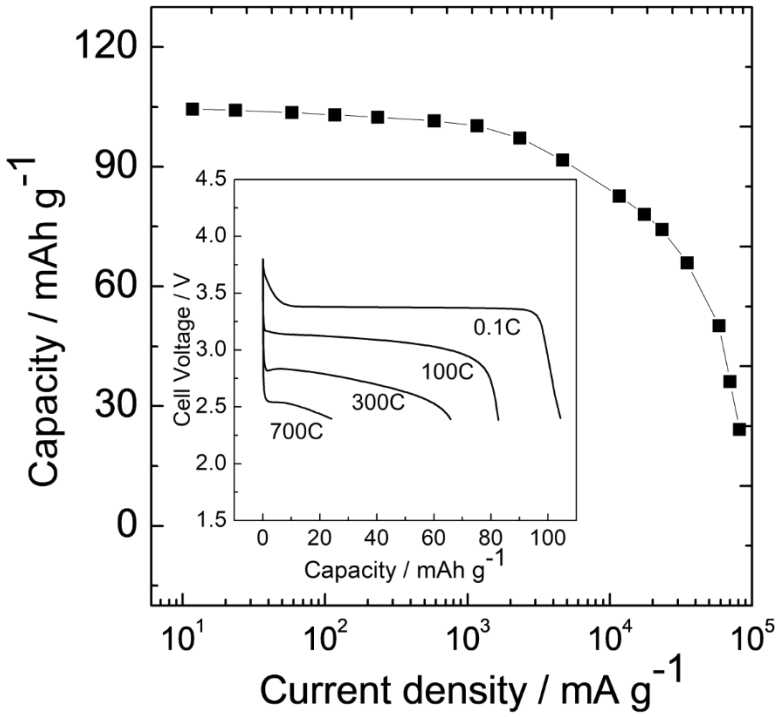

Figure 6 Super-fast Na/NVPC cell rate capability at 363 K. Electrolyte: Na[FSA]-[C_2C_1im][FSA] (Na[FSA] mole fraction = 0.5). Charge rate: 0.1C, discharge rates: 0.1C to 700C, cut-off voltages: 2.4 V/3.8 V. See Table S2 in the Supporting Information for capacity and capacity retention details.

Figure 7 shows electrochemical impedance spectra (EIS) of the Na/NVPC half-cell (Na mole fraction = 0.5) at a state of charge (SOC) of 0.5. EIS results reveal that the interfacial resistance, which is indicated by the high-frequency semicircle (characteristic frequencies of 60–700 Hz) decreases drastically relative to the bulk resistance as the measurement temperature increases. Regarding the charging process, fast charge up to 3.8 V at 100C with Na[FSA] mole fraction of 0.4 at 363 K results in charge capacity of 84.7 mAh g^{-1} (see Figure S9, Supporting Information). However, charging at 100C, followed by further charging at 10C produces a charge capacity of 100.0 mAh g^{-1} in 75 s. Charge–discharge cycles using this charging mode and a 10C discharge process exhibit stable performance over

100 cycles and high Coulombic efficiencies (average >99.9%) (Figure S9, Supporting Information).

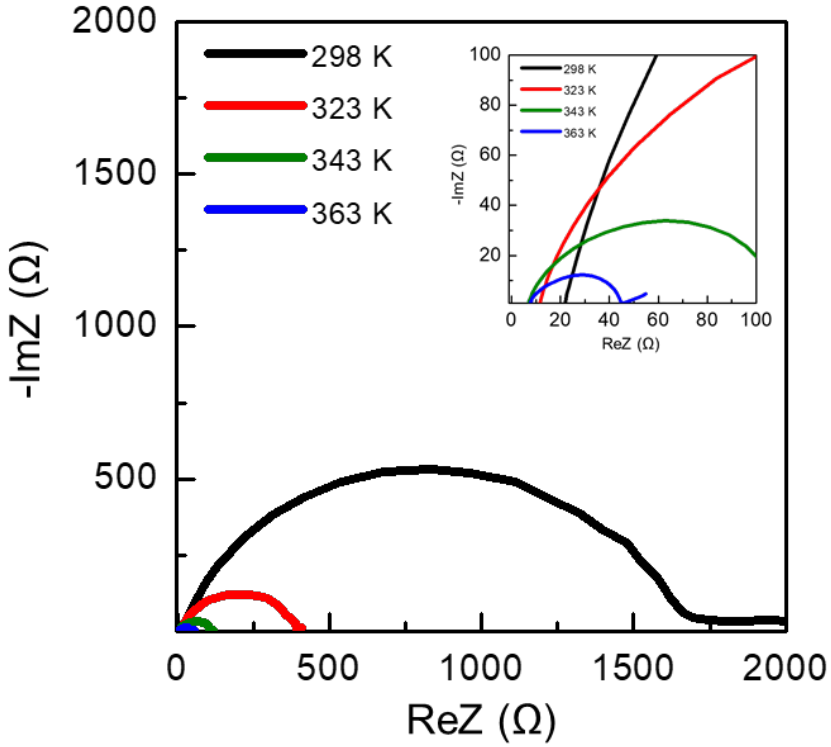

Figure 7 Electrochemical impedance spectra of Na/NVPC cells. Electrolyte: Na[FSA]-[C_2C_1im][FSA] (Na[FSA] mole fraction = 0.5). Temperature: 298−363 K, SOC = 50%, frequency range: 40 mHz – 1000 kHz, AC amplitude: 10 mV.

2.2.3. Cycling Performance

Cycling performance was tested was tested at 298 K and 363 K after the rate capability tests were performed using the same cells with four different Na[FSA] mole fractions. The cells were charged and discharged at 1C for 300 cycles. As shown in **Figure 8**, the NVPC exhibits stable cycling performance at 363 K. In addition, NVPC achieves outstanding capacity retention of 94.8–99.0% after 300 cycles and an average Coulombic efficiency above 99.9% (see Figure S10 in the Supporting Information for the results of measurements performed at 298 K). In Figure 8(e), the long-term cycling performance of a cell based on an IL with an Na[FSA] fraction of 0.4 was tested at 20C. These conditions correspond a charge/discharge cycle time of about 6 min. The cell retains its high capacity for many cycles,

achieving capacity retentions of 96.4%, 92.3%, and 89.2% after the 1000th, 3000th, and 5000th cycles, respectively. Such stable cycling performance is derived from the stable biphasic reaction of NVP and high durability of the IL against redox reactions including Al corrosion and oxidative decomposition.[25]

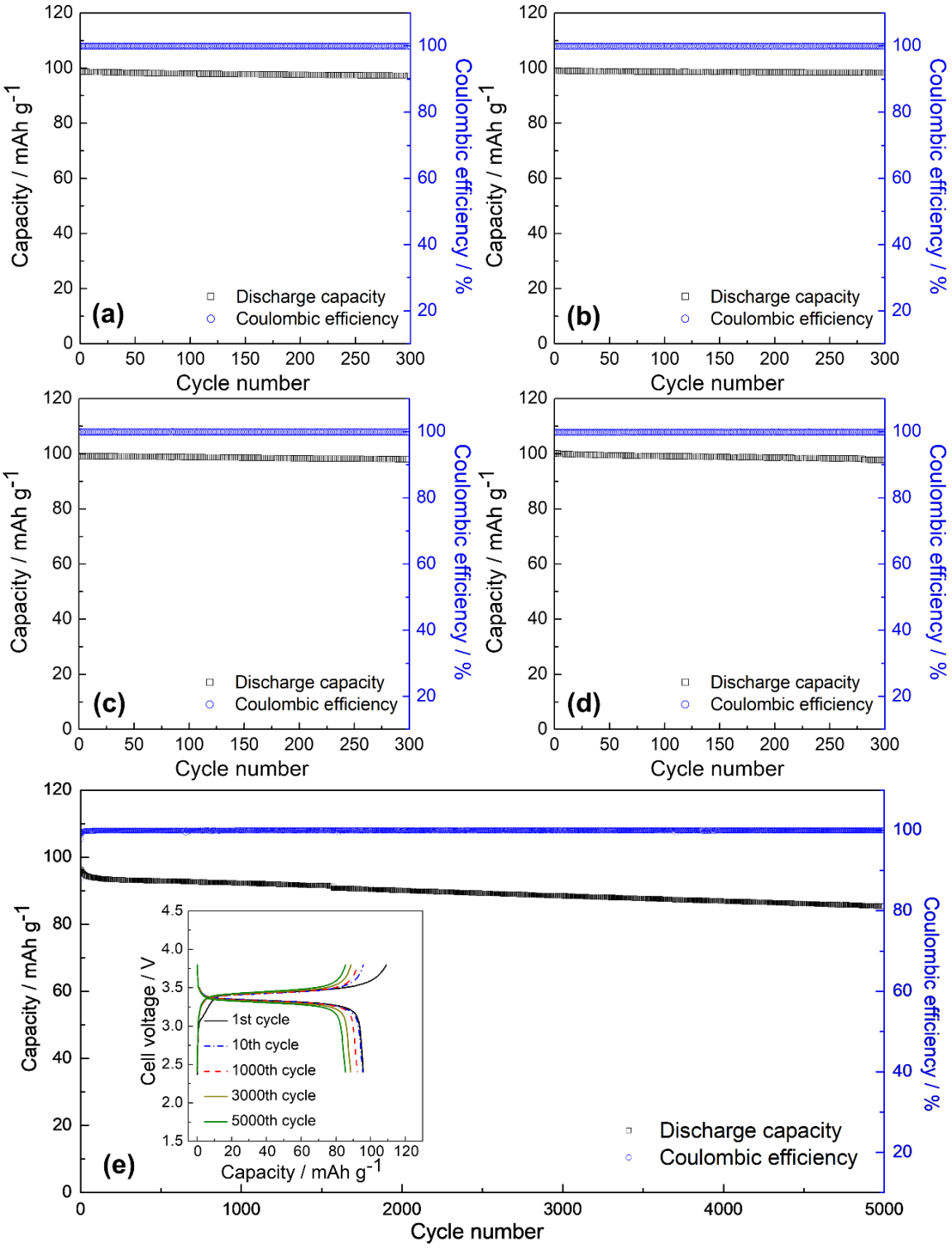

Figure 8 Cycling performance of Na/NVPC cells at 363 K. Electrolyte: Na[FSA]-[C_2C_1im][FSA] with various mole fractions of Na[FSA]. (a) Na[FSA] mole fraction = 0.2, (b) Na[FSA] mole fraction = 0.3, (c) Na[FSA] mole fraction = 0.4, and (d) Na[FSA] mole fraction = 0.5. Charge–discharge rate: 1C for (a)–(d) and 20C for (e). Cut-off voltages: 2.4 V/3.8 V. See Tables S4 and S5 in the Supporting Information for capacity and capacity retention details.

2.2.4. Charge–discharge Behavior Across a Wide Temperature Range

Secondary batteries with the capacity to operate across a wide temperature range have been pursued by various manufacturers. Unfortunately, conventional organic electrolytes limit these batteries to near room-temperature conditions. Additives and co-solvents are required for low-temperature operation, and these electrolytes have difficulty operating above 333 K as a result of safety issues and solid-electrolyte interphase instability.

With regard to low-temperature operation, cells with NVPC positive electrodes and IL electrolytes achieved sufficient electrochemical performance, even at temperatures below the freezing point. **Figure 9** shows the results of charge–discharge measurements of samples with four different mole fractions of Na[FSA] performed below room temperature (298 K, 263 K, 253 K, and 243 K) at 0.1C. Particular attention should be paid to the sample with Na[FSA] mole fraction of 0.2, which exhibits reversible capacities of 100.8 mAh g^{-1}, 78.1 mAh g^{-1}, and 57.6 mAh g^{-1} at 298 K, 263 K, and 253 K, respectively. Since high rate capabilities were observed with high Na[FSA] fractions at intermediate temperatures, optimization of Na[FSA] fraction may be required to match the environment in practical applications.

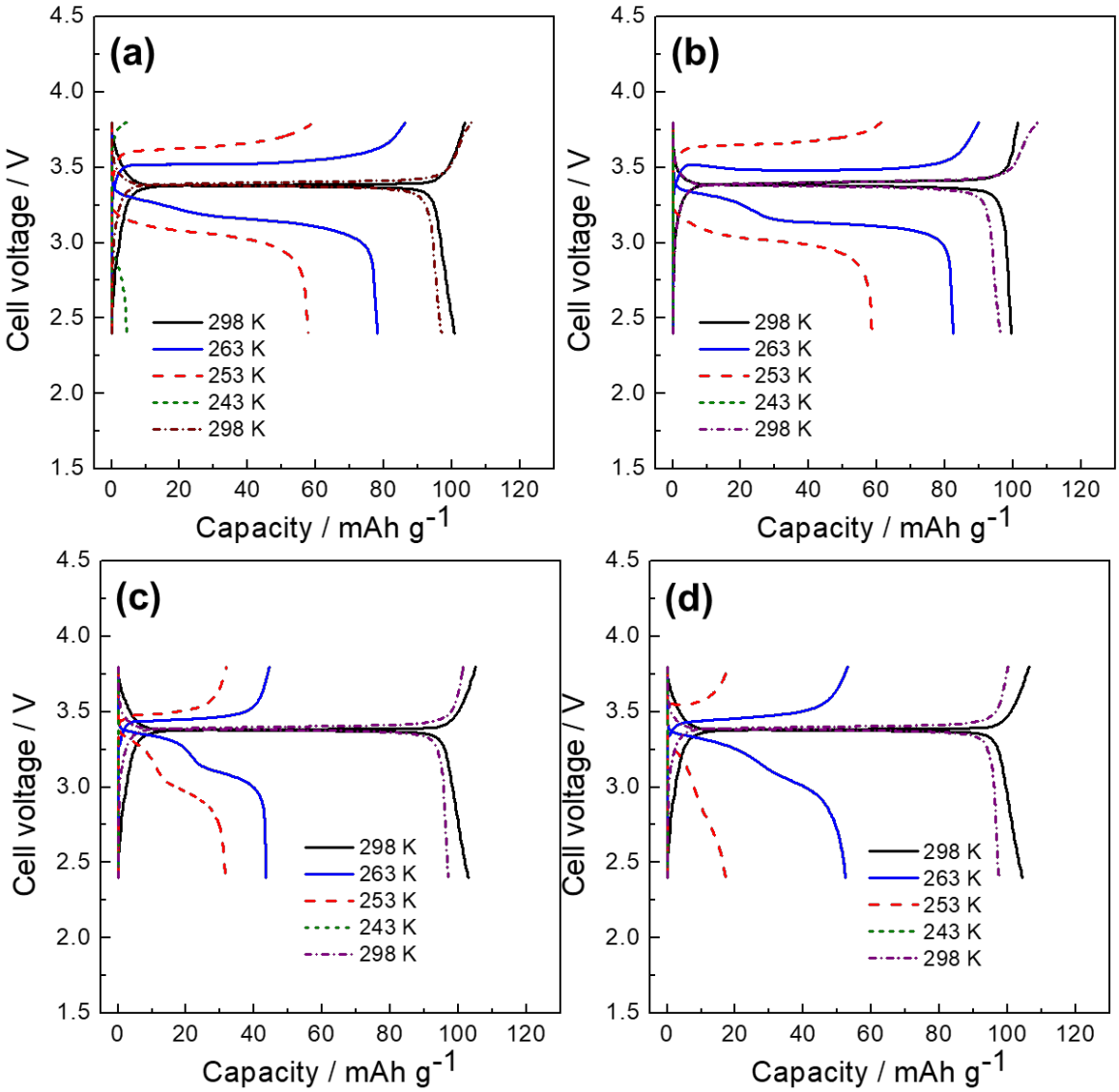

Figure 9 Na/NVPC cell charge-discharge tests conducted at a broad range of temperatures. Electrolytes: Na[FSA]-[C_2C_1im][FSA] with various Na[FSA] fractions. (a) Na[FSA] fraction = 0.2, (b) Na[FSA] fraction = 0.3, (c) Na[FSA] fraction = 0.4, and (d) Na[FSA] fraction = 0.5. Charge-discharge rate: 1C, temperature range: 243–298 K, cut-off voltages: 2.4 V/3.8 V.

2.3. *In-situ* XRD Studies of NVPC

Figure 10 shows the results of *in situ* XRD measurements performed to investigate the structural changes in NVPC during electrochemical cycling at 363 K. The Na/NVPC cell was charged and discharged for two cycles at 0.1C, and XRD patterns were recorded in a 2θ range of 10–60°. For the XRD patterns recorded at 2.4 V and 3.8 V, the potential was maintained using a constant voltage mode during charging and discharging. The other patterns were recorded during the charge–discharge cycles. The diffraction peak at 18.1° is assigned to

PTFE, while those at 38.43° and 44.67° are assigned to the Al current collector. The measured *in-situ* XRD patterns are in good agreement with the Bragg peak positions of NVP and $NaV_2(PO_4)_3$ simulated from previous structural data.[26] When charging begins, the XRD patterns match the pattern of unaltered NVP.[26] As the charging proceeds and de-sodiation from the NVP phase occurs, the XRD spectrum shows the appearance of new peaks and disappearance of old peaks. The XRD pattern after charging to 3.8 V matches the pattern of $NaV_2(PO_4)_3$ prepared chemically by extracting Na^+ from NVP.[26] After the reverse process, the XRD pattern resembles that of the original NVP prepared via sodiation. The applicable Bragg peak position changes appear to be completely reversible for two charge–discharge cycles. The series of XRD patterns of NVPC, collected over two charge–discharge cycles, suggests that Na insertion/extraction occurs in a two-phase manner. Transformation from $NaV_2(PO_4)_3$ to $Na_3V_2(PO_4)_3$ and the reverse process both occur at 363 K. The process is similar to that reported in a previous study, which was conducted at 298 K using a conventional organic electrolyte.[11d]

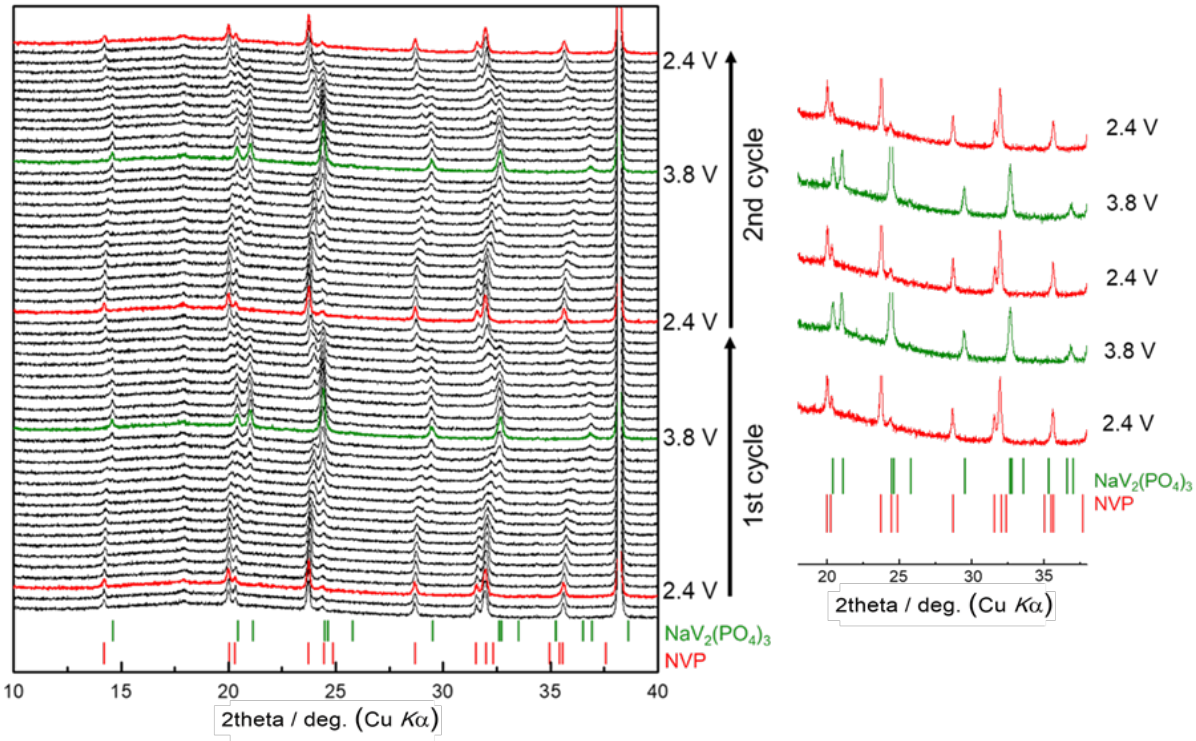

Figure 10 *In-situ* X-ray diffraction patterns of NVPC positive electrode recorded during the first and second charge–discharge cycles at 363 K. Red and green bars indicate simulated

NVP and $NaV_2(PO_4)_3$ Bragg peaks.[26] The peak at 38.3° originates from the Al current collector. Cut-off voltages: 2.4 V/3.8 V, current density: 10 mA g^{-1}.

2.4. Comparison of Power and Energy Densities of Selected Positive Electrode Materials

Figure 11 shows the relationships between energy and power densities for selected positive electrode materials that include FSA-based IL electrolytes ($NaCrO_2$, $NaFeP_2O_7$, and NVPC) at 298 and 363 K. The same conditions were used to determine the performance of each electrode in the present work. Power densities are calculated based on the weight of the positive electrode material, assuming the use of Na metal negative electrode. Na[FSA] mole fractions of 0.3 and 0.5 are used at 298 K, and mole fraction of 0.5 is used at 363 K. Low and high mole fractions of Na[FSA] resulted in better performance at 298 K and 363 K, respectively.[18a, 18b] The $NaCrO_2$ positive electrode material with an average working voltage of ~3.0 V is one of the most widely investigated layered oxides for Na secondary batteries.[27] It exhibits stable charge–discharge behavior at intermediate temperatures with a practical capacity of ~110 mAh g^{-1}.[18c, 28] The pyrophosphate $Na_2FeP_2O_7$ possesses a theoretical capacity of 97 mA g^{-1} and has three-dimensional Na^+ diffusion paths with acceptably low activation energies.[8c, 29] This material exhibits a high rate capability at 363 K and charge–discharge rates of up to 400C.[18b, 22b] Although electrode performance is enhanced by increasing the operating temperature, the comparison in Figure 11 indicates that NVPC performs considerably better than $NaCrO_2$ or $NaFeP_2O_7$. The differences between performance at 298 K and 363 K for NVPC are smaller than those reported for $NaCrO_2$ or $NaFeP_2O_7$. In addition, the energy density delivered by NVPC at a high power density is quite attractive because of its high rate performance. The good performance of NVPC is derived from the combination of high Na^+ ion diffusivity in the NASICON structure and improved electronic conductivity by carbon coating. Furthermore, the intermediate-temperature operation enhances the interfacial process as well as ionic and electronic conductivities, thus

resulting in the relationship between power density and energy density. The higher working voltage of NVPC when compared to those of other materials is also advantageous for high energy density.

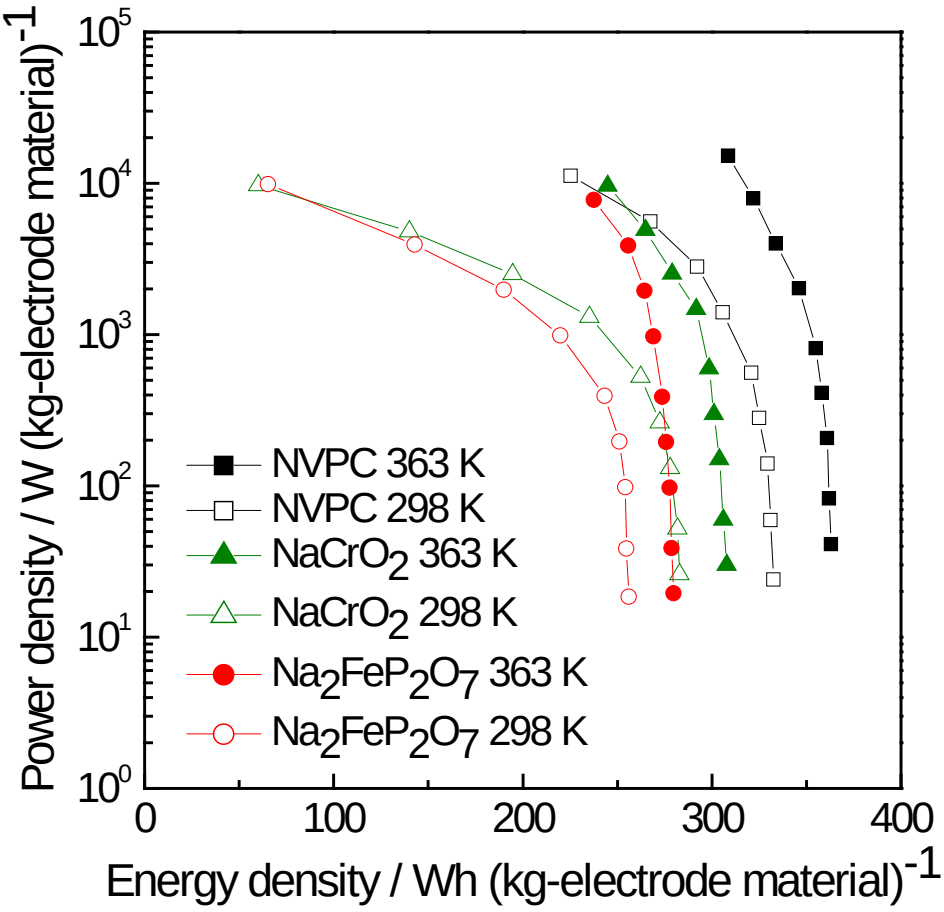

Figure 11 Relationships between power and energy densities for NVPC, $Na_2FeP_2O_7$, and $NaCrO_2$ with Na[FSA]-[C_2C_1im][FSA] IL electrolytes based on rate capability tests (Na[FSA] mole fraction = 0.3 at 298 K and Na[FSA] mole fraction = 0.5 at 363 K). Power and energy densities are calculated based on the weight of the positive electrode, assuming Na metal negative electrode.

3. Conclusions

High rate capabilities, good cycling performance, a wide range of operating temperatures, and good safety characteristics are required for practical Na secondary battery applications. In this work, NVPC composites were prepared via sol-gel chemistry and combined with Na[FSA]-[C_2C_1im][FSA] IL electrolytes to achieve excellent electrochemical performance. The composites exhibited superior reversible charge–discharge performance

across a wide temperature range of 243 K to 363 K. The composites also exhibited good cycling stability over 5000 cycles and outstanding charge/discharge rates under various operating conditions. X-ray diffraction analysis revealed that the charge–discharge process proceeds in a two-phase manner at an elevated temperature (363 K), matching the mechanism previously reported at room temperature. The power and energy densities of various Na/positive electrode ($NaCrO_2$, $Na_2FeP_2O_7$, and NVPC) cells with IL electrolytes were compared, and NVPC delivered the highest energy and power densities. The results demonstrate the outstanding performance of NVPC with a high safety over a wide temperature range. This type of Na secondary battery has potential to be used in various situations such as the ones in ESS and EV which are mentioned above. Furthermore, it enables the potential for practical utilization in non-ambient conditions, particularly hot environments such as in engine compartments or near domestic boilers where latent heat exists. Acceleration of research directed to the use of ionic liquid electrolytes at elevated temperatures is expected in future studies, since it provides an effective way to enable a more sustainable society.

4. Experimental Section

4.1. Synthesis and Characterization

The powdery NVPC was synthesized via a sol-gel method.[11c] In a typical procedure, 1.8185 g of V_2O_5 (Sigma-Aldrich Chemistry, 99.6% purity, 9.998 mmol) and 6.3036 g of oxalic acid dihydrate (Wako Pure Chemical Industries, 99.5–100.2% purity, 50.001 mmol) were dissolved in water, previously subjected to ion exchange treatment, at 353 K via continuous stirring using a magnetic bar. In this reaction, oxalic acid works both as a reducing agent and as a carbon source. As the color of the homogeneous mixture turned blue, 1.1999 g of NaOH (Wako Pure Chemical Industries, 97.0% purity, 30.000 mmol), 3.4510 g of $NH_4H_2PO_4$ (Wako

Pure Chemical Industries, 99.0% purity, 30.002 mmol), and 1.7118 g of glucose (Wako Pure Chemical Industries, 5.001 mmol) were added to the solution and the mixture was stirred for additional 3 h. Glucose was used as a carbon source and vanadium served as the reducing agent. The solution was dried completely at 393 K for a day and then ground using a mortar and pestle. The dry powder was calcined at 623 K for 5 h under a flow of Ar. After calcination, the precursor was ground using a mortar and pestle and heated at 1073 K under the flow Ar for 8 h.

NVP-SS was prepared for comparison via a conventional solid-state method. To this end, 2.98186 g of V_2O_3 (Wako Pure Chemical Industries, >99% purity, 19.895 mmol) and 7.166 g of NaH_2PO_4 (Wako Pure Chemical Industries, >99% purity, 59.727 mmol) were ball-milled in acetone for 12 h at 600 rpm using a Fritsch Pulverisette 7 Premium Line. The mixture was collected and dried under vacuum for 24 h at 393 K and subsequently thoroughly ground using a mortar and pestle. After grinding, the precursor was pelletized (70 MPa) for 10 min. The precursor pellet was heated at 1073 K for 40 h under Ar flow, and then cooled to 298 K. The $NaCrO_2$ and $Na_2FeP_2O_7$ samples were prepared as previously reported.[18a, 18b]

XRD patterns were collected in the Bragg-Brentano geometry using a Rigaku SmartLab diffractometer with Ni-filtered Cu-$K\alpha$ radiation (40 kV and 30 mA) to confirm NVPC purity. The diffractometer was equipped with a silicon strip high-speed detector (Rigaku D/teX Ultra 250). Rietveld refinement was performed using the FullProf software.[30] The NVPC morphology was observed via SEM (Hitachi SU-8020), and EDS mapping was performed using an analyzer (Horiba EMAXEvolution X-max) attached to the SEM. Surface area of the electrode materials was evaluated using the BET method[31] based on the results of nitrogen adsorption analysis performed using Tristar II 3020 (Shimadzu Corp.).

4.2. Electrochemical Measurements

Electrochemical properties were measured using 2032 coin-type cells at 253 to 363 K. A charge/discharge rate of 0.1C was used to understand the basic behavior of each system. Discharge currents ranging from 0.1C to 700C were used in rate capability tests. The cut-off voltages were fixed at 2.4 V/3.8 V. Sodium metal (Sigma-Aldrich Chemistry, 99.95% purity) was cut into a disk (16 mm in diameter) and fixed on an Al plate current collector as the negative electrode. The positive electrode was prepared by mixing the NVPC composite, Super C65, and PTFE (80:15:5, wt%) and pressing the mixture on an Al mesh (the loading mass of the active material in the electrodes is approximately 3 mg cm^{-2}). $NaCrO_2$ and $Na_2FeP_2O_7$ electrodes were prepared in the same manner.[18b, 32] The NVPC sample used for rate capability tests was washed using ion-exchanged water and vacuum-dried at 363 K for 24 h prior to the electrode fabrication. Na[FSA]-[C_2C_1im][FSA] ionic liquids with molar ratios of 20:80, 30:70, 40:60, and 50:50 were used as electrolytes. The salts, Na[FSA] (Mitsubishi Materials Electronic Chemicals, purity >99%) and [C_2C_1im][FSA] (Kanto Chemical, purity >99.9%), were dried under vacuum for 24 h at 353 K. The IL electrolyte was prepared by mixing these two salts at Na[FSA] mole fractions of 0.1, 0.2, 0.3, 0.4, and 0.5. The typical water content of the IL system was below 30 ppm based on Karl–Fischer titration measurements (899 Coulometer, Metrohm). A glass microfiber separator was impregnated with the electrolyte at 333 K under vacuum for 1 day prior to the test. Charge–discharge properties, rate capabilities, and cycling were evaluated using an HJ1001SD8 charge–discharge test device (Hokuto Denko). All electrochemical measurements were started at least 2 h after the relevant temperature adjustments.

Cells were prepared for EIS using 2032 coin-type cells. The cells were assembled in dry Ar. Measurements were performed using a VSP potentiostat (Bio-Logic) at 298 K, 323 K, 343 K, and 363 K over a frequency range from 1 MHz to 40 mHz with a perturbation amplitude of 10 mV.

4.3 *In-situ* XRD Measurements

In-situ XRD measurements were performed using an airtight cell with a Kapton® window and a temperature controller (Rigaku). The diffraction patterns were recorded at 363 K under vacuum. The electrochemical measurements were controlled using an ECAD1000 charge–discharge system (EC Frontier Inc.). The cell was continuously charged and discharged at 10 mA g^{-1} during XRD measurements performed at a scan rate of 1° s^{-1}. The cell voltage was maintained in fully charged and discharged (3.8 V and 2.4 V, respectively) states to confirm the structures in these stable states.

Supporting Information

Supporting Information is available from the Wiley Online Library or from the author.

Acknowledgments

This study was partly supported by Advanced Low Carbon Technology Research and Development Program (ALCA) of the Japan Science and Technology Agency (JST) and Japanese Ministry of Education, Culture, Sports, Science and Technology (MEXT) program "Elements Strategy Initiative to Form Core Research Center".

References

[1] a) A. N. Arnette, *Renewable Sustainable Energy Rev.* **2017**, *70*, 254; b) G. L. Soloveichik, *Annu. Rev. Chem. Biomol. Eng.* **2011**, *2*, 503.

[2] B. Dunn, H. Kamath, J. M. Tarascon, *Science* **2011**, *334*, 928.

[3] B. Scrosati, J. Garche, *J. Power Sources* **2010**, *195*, 2419.

[4] a) J.-M. Tarascon, *Nat. Chem.* **2010**, *2*, 510; b) H. Vikstrom, S. Davidsson, M. Hook, *Appl. Energy* **2013**, *110*, 252.

[5] a) A. Ponrouch, E. Marchante, M. Courty, J. M. Tarascon, M. R. Palacin, *Energy Environ. Sci.* **2012**, *5*, 8572; b) D. Larcher, J. M. Tarascon, *Nat. Chem.* **2015**, *7*, 19; c) M. S. Islam, C. A. Fisher, *Chem. Soc. Rev.* **2014**, *43*, 185; d) N. Yabuuchi, K. Kubota,

M. Dahbi, S. Komaba, *Chem. Rev.* **2014**, *114*, 11636; e) A. Ponrouch, D. Monti, A. Boschin, B. Steen, P. Johansson, M. R. Palacin, *J. Mater. Chem. A* **2015**, *3*, 22; f) A. Ponrouch, R. Dedryvere, D. Monti, A. E. Demet, J. M. A. Mba, L. Croguennec, C. Masquelier, P. Johansson, M. R. Palacin, *Energy Environ. Sci.* **2013**, *6*, 2361; g) K. Kubota, S. Komaba, *J. Electrochem. Soc.* **2015**, *162*, A2538; h) G. G. Eshetu, S. Grugeon, H. Kim, S. Jeong, L. Wu, G. Gachot, S. Laruelle, M. Armand, S. Passerini, *Chem. Sus. Chem.* **2016**, *9*, 462; i) M. D. Slater, D. Kim, E. Lee, C. S. Johnson, *Adv. Funct. Mater.* **2013**, *23*, 947.

[6] N. Yabuuchi, K. Kubota, M. Dahbi, S. Komaba, *Chem. Rev.* **2014**, *114*, 11636.

[7] R. D. Shannon, *Acta Crystallogr. A* **1976**, *32*, 751.

[8] a) A. Whiteside, C. A. Fisher, S. C. Parker, M. S. Islam, *Phys. Chem. Chem. Phys.* **2014**, *16*, 21788; b) Y. Fang, Q. Liu, L. Xiao, X. Ai, H. Yang, Y. Cao, *ACS Appl. Mater. Interfaces* **2015**, *7*, 17977; c) H. Kim, R. A. Shakoor, C. Park, S. Y. Lim, J.-S. Kim, Y. N. Jo, W. Cho, K. Miyasaka, R. Kahraman, Y. Jung, J. W. Choi, *Adv. Funct. Mater.* **2013**, *23*, 1147; d) B. L. Ellis, W. R. M. Makahnouk, Y. Makimura, K. Toghill, L. F. Nazar, *Nat Mater* **2007**, *6*, 749; e) Y. Kawabe, N. Yabuuchi, M. Kajiyama, N. Fukuhara, T. Inamasu, R. Okuyama, I. Nakai, S. Komaba, *Electrochem. Commun.* **2011**, *13*, 1225.

[9] V. Palomares, M. Casas-Cabanas, E. Castillo-Martinez, M. H. Han, T. Rojo, *Energy Environ. Sci.* **2013**, *6*, 2312.

[10] a) Z. Jian, Y. S. Hu, X. Ji, W. Chen, *Adv. Mater.* **2017**, *29*, 1601925; b) S. Y. Lim, H. Kim, R. A. Shakoor, Y. Jung, J. W. Choi, *J. Electrochem. Soc.* **2012**, *159*, A1393; c) Q. Liu, X. Meng, Z. Wei, D. Wang, Y. Gao, Y. Wei, F. Du, G. Chen, *ACS Appl. Mater. Interfaces* **2016**, *8*, 31709; d) Q. Wang, B. Zhao, S. Zhang, X. Gao, C. Deng, *J. Mater. Chem. A* **2015**, *3*, 7732; e) L. S. Plashnitsa, E. Kobayashi, Y. Noguchi, S. Okada, J. Yamaki, *J. Electrochem. Soc.* **2010**, *157*, A536.

[11] a) J. Zhang, Y. Fang, L. Xiao, J. Qian, Y. Cao, X. Ai, H. Yang, *ACS Appl. Mater. Interfaces* **2017**, *9*, 7177; b) W. Shen, H. Li, Z. Guo, C. Wang, Z. Li, Q. Xu, H. Liu, Y. Wang, Y. Xia, *ACS Appl. Mater. Interfaces* **2016**, *8*, 15341; c) H. Li, C. Wu, Y. Bai, F. Wu, M. Wang, *J. Power Sources* **2016**, *326*, 14; d) Z. L. Jian, W. Z. Han, X. Lu, H. X. Yang, Y. S. Hu, J. Zhou, Z. B. Zhou, J. Q. Li, W. Chen, D. F. Chen, L. Q. Chen, *Adv. Energy Mater.* **2013**, *3*, 156; e) Y. Jiang, Z. Z. Yang, W. H. Li, L. C. Zeng, F. S. Pan, M. Wang, X. Wei, G. T. Hu, L. Gu, Y. Yu, *Adv. Energy Mater.* **2015**, *5*, 1402104.

[12] a) X. Lin, M. Salari, L. M. Arava, P. M. Ajayan, M. W. Grinstaff, *Chem. Soc. Rev.* **2016**, *45*, 5848; b) R. A. Guidotti, F. W. Reinhardt, J. Odinek, *J. Power Sources* **2004**, 136, 257.

[13] a) G. G. Eshetu, S. Grugeon, S. Laruelle, S. Boyanov, A. Lecocq, J. P. Bertrand, G. Marlair, *Phys. Chem. Chem. Phys.* **2013**, *15*, 9145; b) S. Wilken, P. Johansson, P. Jacobsson, *Solid State Ionics* **2012**, *225*, 608.

[14] J. M. Tarascon, M. Armand, *Nature* **2001**, *414*, 359.

[15] a) M. Armand, F. Endres, D. R. MacFarlane, H. Ohno, B. Scrosati, *Nat. Mater.* **2009**, *8*, 621; b) L. Chancelier, A. O. Diallo, C. C. Santini, G. Marlair, T. Gutel, S. Mailley, C. Len, *Phys. Chem. Chem. Phys.* **2014**, *16*, 1967; c) G. B. Appetecchi, M. Montanino, S. Passerini, in *Ionic Liquids: Science and Applications*, Vol. 1117, American Chemical Society **2012**, Ch. 4, p. 67; d) D. R. MacFarlane, N. Tachikawa, M. Forsyth, J. M. Pringle, P. C. Howlett, G. D. Elliott, J. H. Davis, M. Watanabe, P. Simon, C. A. Angell, *Energy Environ. Sci.* **2014**, *7*, 232; e) M. Watanabe, M. L. Thomas, S. Zhang, K. Ueno, T. Yasuda, K. Dokko, *Chem. Rev.* **2017**, *117*, 7190.

[16] a) W. Xu, E. I. Cooper, C. A. Angell, *J. Phys. Chem. B* **2003**, *107*, 6170; b) A. Noda, K. Hayamizu, M. Watanabe, *J. Phys. Chem. B* **2001**, *105*, 4603; c) D. R. MacFarlane, M. Forsyth, E. I. Izgorodina, A. P. Abbott, G. Annat, K. Fraser, *Phys. Chem. Chem. Phys.* **2009**, *11*, 4962.

[17] a) G. A. Giffin, *J. Mater. Chem. A* **2016**, *4*, 13378; b) L. Otaegui, E. Goikolea, F. Aguesse, M. Armand, T. Rojo, G. Singh, *J. Power Sources* **2015**, *297*, 168.

[18] a) C. Ding, T. Nohira, R. Hagiwara, K. Matsumoto, Y. Okamoto, A. Fukunaga, S. Sakai, K. Nitta, S. Inazawa, *J. Power Sources* **2014**, *269*, 124; b) C.-Y. Chen, T. Kiko, T. Hosokawa, K. Matsumoto, T. Nohira, R. Hagiwara, *J. Power Sources* **2016**, *332*, 51; c) C. Ding, T. Nohira, K. Kuroda, R. Hagiwara, A. Fukunaga, S. Sakai, K. Nitta, S. Inazawa, *J. Power Sources* **2013**, *238*, 296; d) J. Hwang, K. Matsumoto, Y. Orikasa, M. Katayama, Y. Inada, T. Nohira, R. Hagiwara, *J. Power Sources* **2018,** *377*, 80.

[19] a) T. Yamamoto, T. Nohira, R. Hagiwara, A. Fukunaga, S. Sakai, K. Nitta, *Electrochim. Acta* **2016**, *211*, 234; b) A. Fukunaga, T. Nohira, R. Hagiwara, K. Numata, E. Itani, S. Sakai, K. Nitta, S. Inazawa, *J. Power Sources* **2014**, *246*, 387; c) T. Yamamoto, T. Nohira, R. Hagiwara, A. Fukunaga, S. Sakai, K. Nitta, S. Inazawa, *Electrochim. Acta* **2014**, *135*, 60.

[20] a) M. Ishikawa, T. Sugimoto, M. Kikuta, E. Ishiko, M. Kono, *J. Power Sources* **2006**, *162*, 658; b) H. Matsumoto, H. Sakaebe, K. Tatsumi, M. Kikuta, E. Ishiko, M. Kono, *J. Power Sources* **2006**, *160*, 1308; c) M. Forsyth, H. Yoon, F. Chen, H. Zhu, D. R. MacFarlane, M. Armand, P. C. Howlett, *J. Phys. Chem. C* **2016**, *120*, 4276; d) T. Hosokawa, K. Matsumoto, T. Nohira, R. Hagiwara, A. Fukunaga, S. Sakai, K. Nitta, *J. Phys. Chem. C* **2016**, *120*, 9628; e) I. A. Shkrob, T. W. Marin, Y. Zhu, D. P. Abraham, *J. Phys. Chem. C* **2014**, *118*, 19661.

[21] K. Matsumoto, Y. Okamoto, T. Nohira, R. Hagiwara, *J. Phys. Chem. C* **2015**, *119*, 7648.

[22] a) C.-Y. Chen, K. Matsumoto, T. Nohira, R. Hagiwara, *J. Electrochem. Soc.* **2015**, *162*, A2093; b) C.-Y. Chen, K. Matsumoto, T. Nohira, C. Ding, T. Yamamoto, R. Hagiwara, *Electrochim. Acta* **2014**, *133*, 583; c) T. Yamamoto, T. Nohira, R. Hagiwara, A. Fukunaga, S. Sakai, K. Nitta, S. Inazawa, *Electrochim. Acta* **2014**, *135*, 60.

[23] K. Matsumoto, T. Hosokawa, T. Nohira, R. Hagiwara, A. Fukunaga, K. Numata, E. Itani, S. Sakai, K. Nitta, S. Inazawa, *J. Power Sources* **2014**, *265*, 36.

[24] K. Saravanan, C. W. Mason, A. Rudola, K. H. Wong, P. Balaya, *Adv. Energy Mater.* **2013**, *3*, 444.

[25] a) C. Verma, E. E. Ebenso, M. A. Quraishi, *J. Mol. Liq.* **2017**, *233*, 403; b) E. Cho, J. Mun, O. B. Chae, O. M. Kwon, H. T. Kim, J. H. Ryu, Y. G. Kim, S. M. Oh, *Electrochem. Commun.* **2012**, *22*, 1.

[26] Z. Jian, C. Yuan, W. Han, X. Lu, L. Gu, X. Xi, Y.-S. Hu, H. Li, W. Chen, D. Chen, Y. Ikuhara, L. Chen, *Adv. Funct. Mater.* **2014**, *24*, 4265.

[27] a) S. Komaba, C. Takei, T. Nakayama, A. Ogata, N. Yabuuchi, *Electrochem. Commun.* **2010**, *12*, 355; b) J. J. Braconnier, C. Delmas, P. Hagenmuller, *Mater. Res. Bull.* **1982**, *17*, 993.

[28] C.-Y. Chen, K. Matsumoto, T. Nohira, R. Hagiwara, A. Fukunaga, S. Sakai, K. Nitta, S. Inazawa, *J. Power Sources* **2013**, *237*, 52.

[29] P. Barpanda, G. Liu, C. D. Ling, M. Tamaru, M. Avdeev, S.-C. Chung, Y. Yamada, A. Yamada, *Chem. Mater.* **2013**, *25*, 3480.

[30] J. R.-Carvajal, Commission on powder diffraction (IUCr) *Newsletter* **2001,** *26*, 12.

[31] S. Brunauer, P. H. Emmett, E. Teller, *J. Am. Chem. Soc.* **1938**, *60*, 309.

[32] C.-Y. Chen, K. Matsumoto, T. Nohira, R. Hagiwara, A. Fukunaga, S. Sakai, K. Nitta, S. Inazawa, *J. Power Sources* **2013**, *237*, 52.